Journal of Rock Mechanics and Geotechnical Engineering 14 (2022) 303–314

Contents lists available at ScienceDirect

Journal of Rock Mechanics and Geotechnical Engineering

journal homepage: www.jrmge.cn

Full Length Article

Poroelastic solution of a wellbore in a swelling rock with non-hydrostatic stress field

Mohsen S. Masoudian [a,*], Zhongwei Chen [b], Christopher Leonardi [b]

[a] Beck Engineering Pty. Ltd., Chatswood, New South Wales, 2067, Australia
[b] School of Mechanical and Mining Engineering, The University of Queensland, St. Lucia, Queensland, 4072, Australia

ARTICLE INFO

Article history:
Received 19 January 2021
Received in revised form
29 March 2021
Accepted 9 May 2021
Available online 27 June 2021

Keywords:
Poroelasticity
Coupled geomechanics
Analytical solution
Wellbore
Cavity expansion
Coalbed methane (CBM)

ABSTRACT

The stress distribution around a circular borehole has been studied extensively. The existing analytical poroelastic solutions, however, often neglect the complex interactions between the solid and fluid that can significantly affect the stress solution. This is important in unconventional gas reservoirs such as coalbeds and shale formations. In order to address this limitation, this paper presents the development of a poroelastic solution that takes into account the effect of gas sorption-induced strain. The solution considers drainage of the reservoir fluid through a vertical wellbore in an isotropic, homogenous, poroelastic rock with non-hydrostatic in situ stress field. The sorption-induced shrinkage of coal is modelled using a Langmuir-type curve which relates the volumetric change to the gas pressure. The redistributed stress field around the wellbore after depletion is found by applying Biot's definition of effective stress and Airey's stress functions, which leads to a solution of the inhomogeneous Biharmonic equation. Two sets of boundary conditions were considered in order to simulate the unsupported cavity (open-hole) and supported cavity (lined-hole) cases. The implementation was verified against a numerical solution for both open-hole and lined-hole cases. A comparative study was then conducted to show the significance of the sorption-induced shrinkage in the stress distribution. Finally, a parametric study analysed the sensitivity of the solution to different poroelastic parameters. The results demonstrate that the developed solution is a useful tool that can be employed alongside complex flow models in order to conduct efficient, field-scale coupled hydro-mechanical simulations, especially when the stress-dependent permeability of the reservoir is of concern.

1. Introduction

The problem of stress around a circular cavity in soil and rock has been the focus of many studies from a range of disciplines such as geotechnical engineering and petroleum engineering. A number of analytical solutions based on continuum mechanics have been developed to provide the response of tunnels in poroelastic medium (Sulem et al., 1987; Detournay and Cheng, 1988; Fahimifar et al., 2010; Chen and Yu, 2015), or the deformation of wellbores (Detournay and Cheng, 1988; Zhang et al., 2003; Abousleiman and Nguyen, 2005). Studies have considered the poroelastic response of rock and soil through coupling the pressure term with the undrained behaviour of the medium (Detournay and Cheng, 1988; Atefi-Monfared and Rybicki, 2018). However, in some applications, there exist some complex interactions between solid and fluid, and overlooking them can lead to significant misinterpretation of the stress and strain distribution. Taking into account the interactions between the fluid and the solid is crucial for many applications such as tunnelling in expansive soils (Bobet, 2001), geothermal reservoirs (Rawal and Ghassemi, 2014), and geomechanics of unconventional gas reservoirs (Cui et al., 2007; Ghassemi et al., 2009; Masoudian et al., 2019a). Despite this, only a few studies have considered the more complex solid-fluid interactions in their analytical solutions and therefore, that is the main motivation of this paper.

Unconventional gas resources (e.g. coalbed methane and shale gas) represent approximately 40% of the planet's remaining technically recoverable natural gas (McGlade et al., 2013), and they are increasingly being extracted to meet burgeoning global demands (Masoudian et al., 2019b). In addition, unconventional gas

* Corresponding author.
E-mail addresses: mmasoudian@beck.engineering, mohsen.masoudian@gmail.com (M.S. Masoudian).

Peer review under responsibility of Institute of Rock and Soil Mechanics, Chinese Academy of Sciences.

https://doi.org/10.1016/j.jrmge.2021.05.003

reservoirs are being considered as a host rock for CO_2 sequestration, which may also provide an enhanced gas recovery (EGR) technique (White et al., 2005; Johansson et al., 2012; Masoudian, 2016). Of these reservoirs, coalbeds are the main focus of this paper as the geomechanical aspects of coalbed methane reservoirs are not well understood despite nearly three decades of commercial exploitation. Coal is an organic sedimentary rock that contains varying amounts of elements (predominantly carbon), and has a system of natural orthogonal fractures (with spacing as little as a few millimetres) and a wide range of pore sizes (from few nanometre to a few millimetres) and porosity (Laubach et al., 1998; Masoudian et al., 2013a). The majority of natural gas is stored in an adsorbed state on the internal surface area of the micro-pores in the solid matrix, and some free gas is stored within the fractures. The adsorption and desorption of gas are associated with a volume change in the matrix of coal (e.g. Day et al., 2008), i.e. swelling or shrinkage, respectively. Such sorption-induced volume change can have significant implications for the mechanical behaviour of coalbeds during gas production or injection (Liu et al., 2011; Masoudian et al., 2016). On the other hand, due to the wide range of pore sizes existing in coal, a range of complex mechanisms simultaneously governs the flow of gas within coalbeds (e.g. viscous flow, continuum diffusion, Knudsen diffusion). Other chemo-mechanical interactions have also been reported in the literature such as adsorption-induced softening (Masoudian et al., 2013b, 2014). While numerous numerical models have been used to consider these complex coal-gas interactions, their use is very limited when simulating at the field-scale and coupled with advanced numerical flow models. This is mainly because conducting field-scale, fully-coupled hydro-mechanical simulations can be computationally expensive in unconventional gas reservoirs unless only simplified mechanical (e.g. uniaxial displacement) models are used (e.g. Connell and Detournay, 2009; Liu et al., 2010; Zhang et al., 2015). Therefore, revisiting the existing poroelastic models and developing new analytical solutions are desirable to enable more efficient and more accurate simulations of wellbore behaviour.

There exists a class of equations with fully-coupled approach where the pressure and stress equations are solved simultaneously (Detournay and Cheng, 1988; Wong et al., 2008). However, when dealing with swelling media (e.g. coalbeds), the use of such fully-coupled poroelastic solutions, where the flow equation is solved with constant permeability, is not justified because of the spatial and temporal changes of permeability. Therefore, a partially-coupled approach needs to be considered. Thus, the mechanical model can be coupled semi-analytically to a numerical flow model where the complex flow characteristics of the reservoirs and therefore their time-dependent analyses are considered. Subsequently, the coupling terms can be passed between the flow and the mechanical models in every time-step of the analysis, which increases the accuracy of the model. In this case, the 'quasi-static' mechanical model developed for a stationary pressure distribution is appropriate in each time-step. Developing such a mechanical solution is the objective of this paper, which will result in a less expensive computation of field-scale models as well as providing tools for verification of high-fidelity numerical simulations. In addition, the solution can be further used to develop analytical stress-dependent permeability models (Shi and Durucan, 2004; Pan and Connell, 2012; Sedaghat et al., 2017; Agheshlui et al., 2018), which is of significant importance in unconventional gas reservoirs.

Cui et al. (2007) considered the sorption-induced swelling under an axisymmetric plane-strain condition with hydrostatic in situ stress for elastic solution of stress and displacement in coalbeds. Masoudian et al. (2016) extended this model by considering the gas adsorption-induced softening effect under the same field conditions. Elastoplastic solutions have also been developed for swelling gas reservoirs (Masoudian and Hashemi, 2016; Masoudian et al., 2018) and tunnels in swelling rocks (Zareifard and Fahimifar, 2015). These poroelastic solutions for swelling rocks are limited to isotropic stress field conditions, and the poroelastic solutions developed for non-hydrostatic stress conditions have not considered the fluid sorption-induced swelling or shrinkage. More recently, Zare Reisabadi et al. (2020) modified a set of equations for the stress around a borehole to include the Shi and Durucan (2004) formulation of net effective stress change in coalbeds. This paper adds to this body of work and fills a gap by extending the existing poroelastic solutions, in this instance that by Cui et al. (2007), to non-hydrostatic in situ stress conditions. While this paper primarily focuses on the application of this model to wellbores in coalbeds, the developed analytical solutions can be applied for wellbores in other swelling reservoirs (e.g. gas shales) and tunnels in expansive soils and rocks. An important aspect of the novel model developed in this paper is that unlike most other poroelastic solutions (e.g. Detournay and Cheng, 1988; Wong et al., 2008; Bai and Li, 2009), Laplace transform is not employed and thus no numerical Laplace transform inversion is required. Instead, this study employs the Airey's stress function and gives a solution to the Biharmonic equation, a fourth order partial differential equation, which leads to a relatively simplified final solution.

2. Problem definition and governing equations

Consider a two-dimensional plane-strain problem for a homogenous, isotropic, elastic continuum which occupies the space of $-R_0 \le x \le R_0$ and $-R_0 \le y \le R_0$, and contains a circular hole of radius R_w at the centre, as depicted in Fig. 1. Prior to drilling the wellbore and gas production, the reservoir is under in situ stress condition of σ^0_{xx} and σ^0_{yy}, in x and y directions, respectively, and the initial in situ pore pressure is P_0. The different x and y components of stress indicate the non-hydrostatic in situ stress condition. After gas production, the initial stresses and pore pressure are conserved

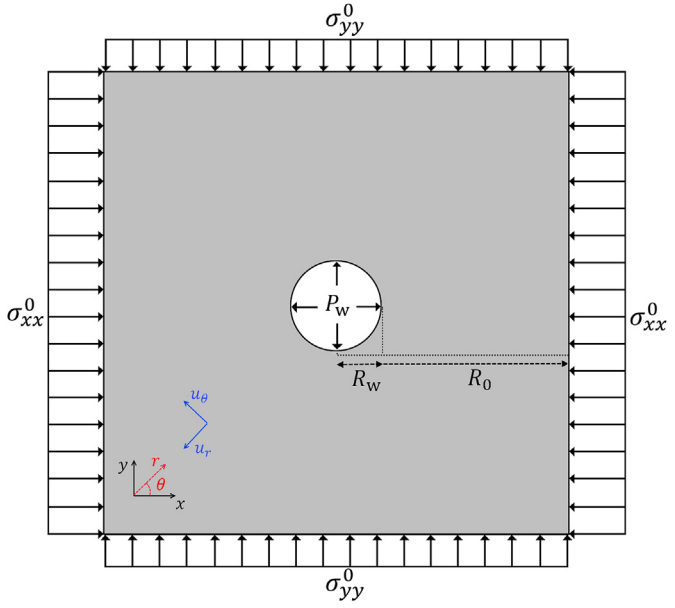

Fig. 1. Geometry and boundary conditions of the problem after gas production (not to scale). The directions of the Cartesian and polar coordinates are also depicted with black and red arrows, respectively, in the bottom left corner. The direction of the positive radial and tangential displacements is depicted with blue arrows. Note that the origin is the centre of the circular hole in the middle for both systems of coordinates.

on the outer boundaries of the model, while the pore pressure on the wellbore wall is P_w. The latter means that the effective stress on the wellbore wall is zero (the total stress is equal to P_w). In order to develop the analytical solution, the following basic assumptions are made in this study:

(1) Reservoir is an isotropic, homogeneous, elastic medium;
(2) Reservoir is saturated by methane;
(3) After gas production, pore pressure distribution reaches a steady state condition;
(4) Matrix swelling can be described by Langmuir-type function;
(5) Swelling/shrinkage is isotropic and occurs instantaneously after pressure increase/decrease in the fractures;
(6) Direction of x and y axes are taken to be the same as the minor and major principal in situ stresses, respectively.

Due to the circular geometry of the hole, it is more convenient to develop the solution in polar coordinates with the origin at the centre of the hole, where compressive stresses are positive, radial displacement towards the wellbore is positive, counter-clockwise tangential displacement is positive, and the sorption-induced swelling is positive (shrinkage is negative), herein. The sorption-induced volumetric change in coal is usually explained with a Langmuir type relationship that relates the swelling strain to pore pressure. Similar to thermal strain where a reference temperature is considered, the swelling strain ($\bar{\varepsilon}_v^s$) is defined by Langmuir's equation for pore pressure with reference to that under in situ conditions:

$$\bar{\varepsilon}_v^s = \frac{\varepsilon_L^s b_L P}{1 + b_L P} - \frac{\varepsilon_L^s b_L P_0}{1 + b_L P_0} \tag{1}$$

where ε_L^s is the maximum swelling coefficient, b_L is the reciprocal of Langmuir pressure, and P is the pore pressure.

The fundamental equations required here are the elastic constitutive equation, the strain compatibility equation, and the equilibrium equation. Considering the plane-strain condition, the Biot definition of effective stress ($\sigma' = \sigma - \alpha P$), and assuming the similarity of swelling strain to thermal strain, the strain-stress equations can be presented as below (Connell, 2009):

$$\varepsilon_{rr} = \frac{1}{E}[\sigma_{rr} - \nu(\sigma_{\theta\theta} + \sigma_{zz}) - (1 - 2\nu)\alpha P] - \frac{\bar{\varepsilon}_v^s}{3} \tag{2a}$$

$$\varepsilon_{\theta\theta} = \frac{1}{E}[\sigma_{\theta\theta} - \nu(\sigma_{zz} + \sigma_{rr}) - (1 - 2\nu)\alpha P] - \frac{\bar{\varepsilon}_v^s}{3} \tag{2b}$$

$$\varepsilon_{zz} = \frac{1}{E}[\sigma_{zz} - \nu(\sigma_{rr} + \sigma_{\theta\theta}) - (1 - 2\nu)\alpha P] - \frac{\bar{\varepsilon}_v^s}{3} = 0 \tag{2c}$$

$$\varepsilon_{r\theta} = \frac{\tau_{r\theta}}{2G} \tag{2d}$$

where ε represents the strain; σ represents the normal stress; τ represents the shear stress; the subscripts r, θ and z indicate the radial, tangential and in-plane directions, respectively; α is the Biot coefficient; E is the elastic modulus; ν is the Poisson's ratio; and G is the shear modulus defined as

$$G = \frac{E}{2(1 + \nu)} \tag{3}$$

Solving Eq. (2c) for σ_{zz} and substituting it into Eqs. (2a) and (2b), the stress-strain equations can be written as

$$\varepsilon_{rr} = \frac{1}{\bar{E}}[\sigma_{rr} - \bar{\nu}\sigma_{\theta\theta} - (1 - \bar{\nu})\alpha P] - \frac{\bar{\varepsilon}_v^s}{3} \tag{4a}$$

$$\varepsilon_{\theta\theta} = \frac{1}{\bar{E}}[\sigma_{\theta\theta} - \bar{\nu}\sigma_{rr} - (1 - \bar{\nu})\alpha P] - \frac{\bar{\varepsilon}_v^s}{3} \tag{4b}$$

$$\varepsilon_{r\theta} = \frac{\tau_{r\theta}}{2G} \tag{4c}$$

where $\bar{E}$ and $\bar{\nu}$ are the plane-strain elastic modulus and Poisson's ratio, respectively, which can be defined as

$$\bar{E} = \frac{E}{1 - \nu^2} \tag{5a}$$

$$\bar{\nu} = \frac{\nu}{1 - \nu} \tag{5b}$$

The strain-displacement relationships are (Timoshenko and Goodier, 1951):

$$\varepsilon_{rr} = \frac{\partial u_r}{\partial r} \tag{6a}$$

$$\varepsilon_{\theta\theta} = \frac{1}{r}\frac{\partial u_\theta}{\partial \theta} + \frac{u_r}{r} \tag{6b}$$

$$\varepsilon_{r\theta} = \frac{1}{2}\left(\frac{1}{r}\frac{\partial u_r}{\partial \theta} + \frac{\partial u_\theta}{\partial r} - \frac{u_\theta}{r}\right) \tag{6c}$$

The strain compatibility equation can be written as

$$\frac{1}{r^2}\frac{\partial^2 \varepsilon_{rr}}{\partial \theta^2} + \frac{\partial^2 \varepsilon_{\theta\theta}}{\partial r^2} - 2\frac{\partial^2 \varepsilon_{r\theta}}{\partial r \partial \theta} - \frac{1}{r}\frac{\partial \varepsilon_{rr}}{\partial r} + \frac{2}{r}\frac{\partial \varepsilon_{\theta\theta}}{\partial r} - \frac{2}{r}\frac{\partial \varepsilon_{r\theta}}{\partial \theta} = 0 \tag{7}$$

The equilibrium equation can be presented as

$$\frac{\partial \sigma_{rr}}{\partial r} + \frac{\sigma_{rr} - \sigma_{\theta\theta}}{r} + \frac{1}{r}\frac{\partial \tau_{r\theta}}{\partial r} = 0 \tag{8a}$$

$$\frac{\partial \tau_{r\theta}}{\partial r} + \frac{2\tau_{r\theta}}{r} + \frac{1}{r}\frac{\partial \sigma_{\theta\theta}}{\partial \theta} = 0 \tag{8b}$$

The constitutive equation and compatibility equations can be combined to give the new compatibility equation. Substituting the stress-strain relationships into the strain compatibility equation gives the new compatibility equation as

$$\begin{aligned}
&\frac{1}{r^2}\left(\frac{\partial^2 \sigma_{rr}}{\partial \theta^2} - \bar{\nu}\frac{\partial^2 \sigma_{\theta\theta}}{\partial \theta^2}\right) + \frac{\partial^2 \sigma_{\theta\theta}}{\partial r^2} - \bar{\nu}\frac{\partial^2 \sigma_{rr}}{\partial r^2} - \frac{1}{r}\left(\frac{\partial \sigma_{rr}}{\partial r} - \bar{\nu}\frac{\partial \sigma_{\theta\theta}}{\partial r}\right) \\
&+ \frac{2}{r}\left(\frac{\partial \sigma_{\theta\theta}}{\partial r} - \bar{\nu}\frac{\partial \sigma_{rr}}{\partial r}\right) - 2(1 + \bar{\nu})\left(\frac{1}{r^2}\frac{\partial \tau_{r\theta}}{\partial \theta} + \frac{1}{r}\frac{\partial^2 \tau_{r\theta}}{\partial r \partial \theta}\right) \\
&= (1 - \bar{\nu})\alpha\left(\frac{\partial^2 P}{\partial r^2} + \frac{1}{r}\frac{\partial P}{\partial r}\right) + \frac{\bar{E}}{3}\left(\frac{\partial^2 \bar{\varepsilon}_v^s}{\partial r^2} + \frac{1}{r}\frac{\partial \bar{\varepsilon}_v^s}{\partial r}\right)
\end{aligned} \tag{9}$$

An effective way of dealing with mechanical problems is the use of Airey's stress function, which significantly simplifies the solution procedure compared to working with Navier's equation. The stresses can be defined in terms of Airey's stress function (Φ) as

$$\sigma_{rr} = \frac{1}{r}\frac{\partial \Phi}{\partial r} + \frac{1}{r^2}\frac{\partial^2 \Phi}{\partial \theta^2} \tag{10a}$$

$$\sigma_{\theta\theta} = \frac{\partial^2 \Phi}{\partial r^2} \tag{10b}$$

$$\tau_{r\theta} = -\frac{\partial}{\partial r}\left(\frac{1}{r}\frac{\partial \Phi}{\partial \theta}\right) \tag{10c}$$

Note that this equation automatically satisfies the equilibrium equation (Eqs. (8a) and (8b)). Substituting these into the new compatibility equation (Eq. (9)) and using the polar definition of the Laplacian operator (∇^2) gives

$$\nabla^4 \Phi = \nabla^2 \nabla^2 \Phi = (1-\overline{\nu})\alpha \nabla^2 P + \frac{\overline{E}}{3}\nabla^2\left(\overline{\varepsilon}_{\mathrm{v}}^{\mathrm{s}}\right) \tag{11}$$

This is the Biharmonic equation which is a fundamental equation in the theory of elasticity. Note that this equation remains valid for plane-stress but the E and ν are replaced with E and ν, respectively. The Laplacian and Biharmonic operators are defined as

$$\nabla^2\nabla^2\Phi = \nabla^4\Phi = \left(\frac{\partial^2}{\partial r^2}+\frac{1}{r}\frac{\partial}{\partial r}+\frac{1}{r^2}\frac{\partial^2}{\partial \theta^2}\right)\left(\frac{\partial^2}{\partial r^2}+\frac{1}{r}\frac{\partial}{\partial r}+\frac{1}{r^2}\frac{\partial^2}{\partial \theta^2}\right)\Phi \tag{12a}$$

$$\nabla^2 P = \left(\frac{\partial^2 P}{\partial r^2}+\frac{1}{r}\frac{\partial P}{\partial r}+\frac{1}{r^2}\frac{\partial^2 P}{\partial \theta^2}\right) = \frac{\partial^2 P}{\partial r^2}+\frac{1}{r}\frac{\partial P}{\partial r} = \frac{1}{r}\frac{\partial}{\partial r}\left(r\frac{\partial P}{\partial r}\right) \tag{12b}$$

$$\nabla^2 \overline{\varepsilon}_{\mathrm{v}}^{\mathrm{s}} = \left(\frac{\partial^2 \varepsilon_{\mathrm{v}}^{\mathrm{s}}}{\partial r^2}+\frac{1}{r}\frac{\partial \varepsilon_{\mathrm{v}}^{\mathrm{s}}}{\partial r}+\frac{1}{r^2}\frac{\partial^2 \varepsilon_{\mathrm{v}}^{\mathrm{s}}}{\partial \theta^2}\right) = \frac{\partial^2 \overline{\varepsilon}_{\mathrm{v}}^{\mathrm{s}}}{\partial r^2}+\frac{1}{r}\frac{\partial \overline{\varepsilon}_{\mathrm{v}}^{\mathrm{s}}}{\partial r} = \frac{1}{r}\frac{\partial}{\partial r}\left(r\frac{\partial \overline{\varepsilon}_{\mathrm{v}}^{\mathrm{s}}}{\partial r}\right) \tag{12c}$$

Note that pore pressure and swelling strain are taken as radial functions, which means that their values are independent of the tangential direction (θ), hence the derivatives with respect to θ in the Laplacian operator vanish.

3. Solution of stress and displacement

If Eq. (11) is solved for Φ, the stress solution can be found using Eqs. (10a)–(10c). While direct solution of this non-homogeneous Biharmonic equation is complicated, a simplified assumption can assist the process. The assumption is that the stress function after drilling the wellbore and production has the same form as the initial stresses, as suggested by Jussila (1997). Since the x and y directions are chosen the same as the directions of the principal stresses, the initial in situ stresses can be written in polar coordinates as below (Jussila, 1997):

$$\sigma_{rr}^0 = \frac{1}{2}\left(\sigma'^0_{xx}+\sigma'^0_{yy}\right)+\frac{1}{2}\left(\sigma'^0_{xx}-\sigma'^0_{yy}\right)\cos(2\theta)+\alpha P_0 \tag{13a}$$

$$\sigma_{\theta\theta}^0 = \frac{1}{2}\left(\sigma'^0_{xx}+\sigma'^0_{yy}\right)-\frac{1}{2}\left(\sigma'^0_{xx}-\sigma'^0_{yy}\right)\cos(2\theta)+\alpha P_0 \tag{13b}$$

$$\tau_{r\theta}^0 = -\frac{1}{2}\left(\sigma'^0_{xx}-\sigma'^0_{yy}\right)\sin(2\theta) \tag{13c}$$

Note that in Eqs. (13a)–(13c), the in situ stresses have been decomposed into its effective stress and pressure components according to the Biot's definition. Assuming that the stress function after drilling the wellbore and production has the same form as the initial stresses, the stress function can then be chosen as

$$\Phi = f_1(r)+f_2(r)\cos(2\theta)+(1-\overline{\nu})\alpha f_{\mathrm{p}}[P(r)]+\frac{\overline{E}}{3}f_{\mathrm{s}}\left[\overline{\varepsilon}_{\mathrm{v}}^{\mathrm{s}}(r)\right] \tag{14}$$

where f_1, f_2, f_{p} and f_{s} are some unknown functions describing the effects of the first stress invariant (hydrostatic), the second stress invariant (deviatoric), pore pressure, and sorption-induced swelling, respectively. Hereon, the problem is reduced to finding each of these four unknown functions. Substituting the stress function of Eq. (14) into Eq. (11) gives four fourth order differential equations as below (see Appendix A for derivation):

$$\frac{\partial^4 f_1(r)}{\partial r^4}+\frac{2}{r}\frac{\partial^3 f_1(r)}{\partial r^3}-\frac{1}{r^2}\frac{\partial^2 f_1(r)}{\partial r^2}+\frac{1}{r^3}\frac{\partial f_1(r)}{\partial r} = 0 \tag{15a}$$

$$\frac{\partial^4 f_2(r)}{\partial r^4}+\frac{2}{r}\frac{\partial^3 f_2(r)}{\partial r^3}-\frac{9}{r^2}\frac{\partial^2 f_2(r)}{\partial r^2}+\frac{9}{r^3}\frac{\partial f_2(r)}{\partial r} = 0 \tag{15b}$$

$$\frac{\partial^4 f_{\mathrm{p}}(r)}{\partial r^4}+\frac{2}{r}\frac{\partial^3 f_{\mathrm{p}}(r)}{\partial r^3}-\frac{1}{r^2}\frac{\partial^2 f_{\mathrm{p}}(r)}{\partial r^2}+\frac{1}{r^3}\frac{\partial f_{\mathrm{p}}(r)}{\partial r} = \frac{\partial^2 P}{\partial r^2}+\frac{1}{r}\frac{\partial P}{\partial r} \tag{15c}$$

$$\frac{\partial^4 f_{\mathrm{s}}(r)}{\partial r^4}+\frac{2}{r}\frac{\partial^3 f_{\mathrm{s}}(r)}{\partial r^3}-\frac{1}{r^2}\frac{\partial^2 f_{\mathrm{s}}(r)}{\partial r^2}+\frac{1}{r^3}\frac{\partial f_{\mathrm{s}}(r)}{\partial r} = \frac{\partial^2 \overline{\varepsilon}_{\mathrm{v}}^{\mathrm{s}}}{\partial r^2}+\frac{1}{r}\frac{\partial \overline{\varepsilon}_{\mathrm{v}}^{\mathrm{s}}}{\partial r} \tag{15d}$$

The general solution of the first two expressions can be found by expansion of the Laplace operator and integration:

$$f_1(r) = A_1 \ln r + B_1 r^2 \ln r + C_1 r^2 + D_1 \tag{16a}$$

$$f_2(r) = A_2 r^2 + B_2 + \frac{C_2}{r^2} \tag{16b}$$

where A_1, A_2, B_1, B_2, C_1, C_2 and D_1 are the integration constants. These two are in fact special cases of the general solution of the Biharmonic equation by Malvern (1969).

For $f_{\mathrm{p}}(r)$ and $f_{\mathrm{s}}(r)$, the problem reduces to solving the following equations, noting the substitution of the Laplace operator definition:

$$\nabla^4 f_{\mathrm{p}}(r) = \frac{1}{r}\frac{\partial}{\partial r}\left\{r\frac{\partial}{\partial r}\left[\nabla^2 f_{\mathrm{p}}(r)\right]\right\} = \frac{1}{r}\frac{\partial}{\partial r}\left(r\frac{\partial P}{\partial r}\right) \tag{17a}$$

$$\nabla^4 f_{\mathrm{s}}(r) = \frac{1}{r}\frac{\partial}{\partial r}\left\{r\frac{\partial}{\partial r}\left[\nabla^2 f_{\mathrm{s}}(r)\right]\right\} = \frac{1}{r}\frac{\partial}{\partial r}\left(r\frac{\partial \overline{\varepsilon}_{\mathrm{v}}^{\mathrm{s}}}{\partial r}\right) \tag{17b}$$

The general solution for these two equations can be found by successive integration of both sides (see Appendix B for details):

$$f_{\mathrm{p}}(r) = \int \frac{1}{r}F_{\mathrm{p}}(r)\mathrm{d}r + A_{\mathrm{p}}\frac{r^2}{4}(\ln r - 1) + B_{\mathrm{p}}\frac{r^2}{4} + C_{\mathrm{p}} \ln r + D_{\mathrm{p}} \tag{18a}$$

$$f_{\mathrm{s}}(r) = \int \frac{1}{r}F_{\varepsilon}(r)\mathrm{d}r + A_{\mathrm{s}}\frac{r^2}{4}(\ln r - 1) + B_{\mathrm{s}}\frac{r^2}{4} + C_{\mathrm{s}} \ln r + D_{\mathrm{s}} \tag{18b}$$

where

$$F_{\mathrm{p}}(r) = \int_{R_{\mathrm{w}}}^{r} P\rho\mathrm{d}\rho \tag{19a}$$

$$F_\varepsilon(r) = \int_{R_w}^{r} \bar{\varepsilon}_v^s \rho \mathrm{d}\rho \tag{19b}$$

where A_p, A_s, B_p, B_s, C_p, C_s, D_p and D_s are the integration constants, with subscripts p and s representing the relevance to pore pressure and swelling terms, respectively. Substituting these four solutions (Eqs. (16a), (16b), (18a) and (18b)) into Airey's representation of stresses (Eqs. (10a)–(10c)) gives (see Appendix C for details):

$$\sigma_{rr} = \frac{A_1}{r^2} + B_1(1+2\ln r) + 2C_1 - \left(2A_2 + \frac{4B_2}{r^2} + \frac{6C_2}{r^4}\right)\cos(2\theta) + \frac{(1-\bar{\nu})\alpha}{r}\frac{\partial f_p(r)}{\partial r} + \frac{\bar{E}}{3r}\frac{\partial f_s(r)}{\partial r} \tag{20a}$$

$$\sigma_{\theta\theta} = -\frac{A_1}{r^2} + B_1(3+2\ln r) + 2C_1 + \left(2A_2 + \frac{6C_2}{r^4}\right)\cos(2\theta) + (1-\bar{\nu})\alpha\frac{\partial^2 f_p(r)}{\partial r^2} + \frac{\bar{E}}{3}\frac{\partial^2 f_s(r)}{\partial r^2} \tag{20b}$$

$$\tau_{r\theta} = \left(2A_2 - \frac{2B_2}{r^2} - \frac{6C_2}{r^4}\right)\sin(2\theta) \tag{20c}$$

It can be further shown that

$$\sigma_{rr} = \frac{A_1}{r^2} + B_1(1+2\ln r) + 2C_1 - \left(2A_2 + \frac{4B_2}{r^2} + \frac{6C_2}{r^4}\right)\cos(2\theta) + \frac{(1-\bar{\nu})\alpha}{r^2}\left[F_p(r) + A_p\frac{r^2}{4}(2\ln r - 1) + B_p\frac{r^2}{2} + C_p\right] + \frac{\bar{E}}{3r^2}\left[F_\varepsilon(r) + A_s\frac{r^2}{4}(2\ln r - 1) + B_s\frac{r^2}{2} + C_s\right] \tag{21a}$$

$$\sigma_{\theta\theta} = -\frac{A_1}{r^2} + B_1(3+2\ln r) + 2C_1 + \left(2A_2 + \frac{6C_2}{r^4}\right)\cos(2\theta) + \frac{(1-\bar{\nu})\alpha}{r^2}\left[r^2P - F_p(r) + A_p\frac{r^2}{4}(2\ln r + 1) + B_p\frac{r^2}{2} - C_p\right] + \frac{\bar{E}}{3r^2}\left[r^2\bar{\varepsilon}_v^s - F_\varepsilon(r) + A_s\frac{r^2}{4}(2\ln r + 1) + B_s\frac{r^2}{2} - C_s\right] \tag{21b}$$

$$\tau_{r\theta} = \left(2A_2 - \frac{2B_2}{r^2} - \frac{6C_2}{r^4}\right)\sin(2\theta) \tag{21c}$$

Since the stresses should be finite at $r >> R_w$ (i.e. $r = R_0$), all the coefficients of the logarithmic terms should be zero, i.e. $B_1 = A_p = A_s = 0$. Knowing that the in situ stress state is conserved at the far field, $r = R_0$, the expression for σ_{rr} from Eqs. (21a) and (13a) can be equated term by term to give the following (the swelling term is equated to zero to account for the constant pore pressure condition on the outer boundary):

$$C_1 = \frac{1}{4}\left(\sigma'^0_{xx} + \sigma'^0_{yy}\right) \tag{22a}$$

$$A_2 = -\frac{1}{4}\left(\sigma'^0_{xx} - \sigma'^0_{yy}\right) \tag{22b}$$

Furthermore, a number of parameters can be defined to simplify the presentation of equations:

$$A = \frac{2A_1}{\sigma'^0_{xx} + \sigma'^0_{yy}} \tag{23a}$$

$$B = \frac{2B_2}{\sigma'^0_{xx} - \sigma'^0_{yy}} \tag{23b}$$

$$C = \frac{2C_2}{\sigma'^0_{xx} - \sigma'^0_{yy}} \tag{23c}$$

$$S_1 = \frac{1}{2}\left(\sigma'^0_{xx} + \sigma'^0_{yy}\right) \tag{23d}$$

$$S_2 = \frac{1}{2}\left(\sigma'^0_{xx} - \sigma'^0_{yy}\right) \tag{23e}$$

Substituting Eqs. (23a)–(23e) into Eqs. (21a)–(21c), the final form of the stress solution can be written as below:

$$\sigma_{rr} = S_1\left(1 + \frac{A}{r^2}\right) + S_2\left(1 - \frac{4B}{r^2} - \frac{6C}{r^4}\right)\cos(2\theta) + \frac{(1-\bar{\nu})\alpha}{r^2}\left[F_p(r) + B_p\frac{r^2}{2} + C_p\right] + \frac{\bar{E}}{3r^2}\left[F_\varepsilon(r) + B_s\frac{r^2}{2} + C_s\right] \tag{24a}$$

$$\sigma_{\theta\theta} = S_1\left(1 - \frac{A}{r^2}\right) - S_2\left(1 - \frac{6C}{r^4}\right)\cos(2\theta) + \frac{(1-\bar{\nu})\alpha}{r^2}\left[r^2P - F_p(r) + B_p\frac{r^2}{2} - C_p\right] + \frac{\bar{E}}{3r^2}\left[r^2\bar{\varepsilon}_v^s - F_\varepsilon(r) + B_s\frac{r^2}{2} - C_s\right] \tag{24b}$$

$$\tau_{r\theta} = -S_2\left(1 + \frac{2B}{r^2} + \frac{6C}{r^4}\right)\sin(2\theta) \tag{24c}$$

Combining Eqs. (4a)–(4c) and (6a)–(6c) and using the final solution of stress as above (Eqs. (24a)–(24c)), the displacement solution can be found as

$$u_r = \frac{r}{\bar{E}}\left\{S_1\left[(1-\bar{\nu}) - (1+\bar{\nu})\frac{A}{r^2}\right] + S_2\left[(1+\bar{\nu})\left(1 + \frac{2C}{r^4}\right) + \frac{4B}{r^2}\right]\cdot\cos(2\theta) + \frac{(1-\bar{\nu})\alpha}{r^2}\left[-(1+\bar{\nu})F_p(r) + (1-\bar{\nu})B_p\frac{r^2}{2} + (1+\bar{\nu})C_p\right] + \frac{\bar{E}}{3r^2}\left[-(1+\bar{\nu})F_\varepsilon(r) + (1-\bar{\nu})B_s\frac{r^2}{2} + (1+\bar{\nu})C_s\right]\right\} \tag{25a}$$

$$u_\theta = \frac{rS_2}{\bar{E}}\left[(1+\bar{\nu})\left(1 - \frac{2C}{r^4}\right) - (1-\bar{\nu})\frac{2B}{r^2}\right]\sin(2\theta) \tag{25b}$$

Eqs. (24a)–(24c), (25a) and (25b) are the final form of the general solution to the stress and displacement around a circular hole. Evaluation of the integration constants is dependent on the chosen boundary conditions. One boundary condition here prescribes that the original in situ stress state is conserved at the far field ($r = R_0$). For the boundary condition on the wall of the wellbore ($r = R_w$), the radial stress at the wellbore wall is equal to the wellbore pressure, i.e. zero effective stress (for open-hole case) and the shear stress is assumed to vanish at the wellbore wall, i.e. $\tau_{r\theta}|_{r=R_w} = 0$ (for both cases). These boundary conditions can be written as

$$\sigma_{rr}|_{r=R_0} = \sigma^0_{rr} \tag{26a}$$

$$\sigma_{\theta\theta}|_{r=R_0} = \sigma^0_{\theta\theta} \tag{26b}$$

$$\tau_{r\theta}|_{r=R_0} = \tau^0_{r\theta} \tag{26c}$$

$$\tau_{r\theta}|_{r=R_w} = 0 \tag{26d}$$

$$\sigma_{rr}|_{r=R_w} = P_w \quad \text{(open-hole)} \tag{26e}$$

$$u_r|_{r=R_w} = 0 \quad \text{(lined-hole)} \tag{26f}$$

When solving these equations for the integration constants, it should be noted that the pore pressure and swelling terms in the radial stress expression need to be equated to the value of pore pressure at the boundaries and zero, respectively. This means that the integration constants within the pore pressure term (B_p and C_p) and the swelling term (B_s and C_s) remain the same for both open-hole and lined-hole cases, while the integration constants within the effective stress term (A, B and C) are different. Solving these equations leads to the following expressions for the integration constants for pressure and swelling terms:

$$B_p = \frac{2}{R_0^2}\left[\frac{R_0^2 P_0}{1-\bar{\nu}} - F_p(R_0) - C_p\right] \tag{27a}$$

$$C_p = \frac{R_0^2 R_w^2}{R_0^2 - R_w^2}\left[-\frac{P_0 - P_w}{1-\bar{\nu}} + \frac{F_p(R_0)}{R_0^2} - \frac{F_p(R_w)}{R_w^2}\right] \tag{27b}$$

$$B_s = \frac{2}{R_0^2}\left[-F_p(R_0) - C_s\right] \tag{27c}$$

$$C_s = \frac{R_0^2 R_w^2}{R_0^2 - R_w^2}\left[\frac{F_p(R_0)}{R_0^2} - \frac{F_p(R_w)}{R_w^2}\right] \tag{27d}$$

The remaining integration constants for the open-hole case are

$$A = -R_w^2 \tag{28a}$$

$$B = R_w^2 \tag{28b}$$

$$C = -\frac{R_w^4}{6}\left(1 + \frac{2B}{R_w^2}\right) \tag{28c}$$

4. Results and discussion

In order to quantitatively analyse the developed solution, values given in Table 1 were assigned to model parameters. These values are predominantly typical of Australian black coal (bituminous or sub-bituminous). These values are first used for verification of the analytical solution by comparing its results with the results of a numerical model. Then, the results of an illustrative example are presented followed by a parametric study which is conducted by independently changing the values to better understand their contribution to the analytical solution of stress distribution around the circular hole. Note that the wellbore pressure is selected to be 6 MPa in the verification phase to ease the convergence of the numerical model, while for the illustrative example, the wellbore pressure is 0.1 MPa. Choosing a low wellbore pressure in the numerical model will require a much finer mesh around the wellbore which requires a large memory and applying larger mesh negatively affects the accuracy and convergence of the mechanical analysis scheme in COMSOL. It should be noted that the main objective of this paper is to present the development of the poroelastic solution, for which a simplified steady-state radial pore pressure solution is used with constant pressures at the wellbore and the outer boundary (P_w and P_0, respectively). The pressure profile takes a logarithmic form as (Cui et al., 2007):

Table 1
Input parameters for the illustrative example.

Parameter	Symbol	Value	Unit
Young's modulus	E	3	GPa
Poisson's ratio	ν	0.3	
Biot's coefficient	α	1	
Wellbore radius	R_w	0.1	m
Outer radius	R_0	10	m
Langmuir's isotherm constant	b_L	0.33	MPa^{-1}
Maximum sorption-induced swelling	ε^s_L	1	%
In situ stress in x direction	σ^0_x	25	MPa
In situ stress in y direction	σ^0_y	20	MPa
Initial reservoir pressure	P_0	10	MPa
Wellbore pressure	P_w	0.1	MPa

Note: Parameters are chosen within the range of those in Masoudian and Hashemi (2016). Wellbore pressure is 6 MPa in verification stage to assist the convergence of the numerical model.

$$P = P_0 + \frac{P_0 - P_w}{\ln(R_0/R_w)}\ln\left(\frac{r}{R_0}\right) \tag{29}$$

4.1. Verification of the analytical solution

The developed analytical solution can be verified against the results of a numerical model. The numerical model was built with COMSOL Multiphysics (a finite element analysis code) using the values presented in Table 1. Two cases of open-hole and lined-hole were constructed to enable the cross-comparison of the results with the analytical solution and the two sets of boundary conditions. The model was constructed as a two-dimensional problem with a square domain representing the reservoir with a circle in the middle representing the wellbore. The length of the rock domain was selected to be 100 times larger than the wellbore diameter. The solid mechanics and Darcy's law physics modules were selected for the model. For the Darcy's law module, a steady-state solution with incompressible fluid was selected, and hence the flow properties (e.g. permeability, porosity, and fluid compressibility) do not affect the pressure solution (though some typical values for flow properties were selected) but the boundary conditions were selected as constant pressure at the wellbore wall and the outer boundary as depicted in Fig. 1. For the solid mechanics module, a linear elastic material was selected with pore pressure as the body load (the gradient of pore pressure calculated from Darcy's law is used as the force per unit volume). The boundary conditions were specified as constant boundary load equivalent to the effective stress (i.e. the solid mechanics module would solve for effective stress); that is boundary load of σ'^0_{xx} on the side boundaries and σ'^0_{yy} on the top and the bottom of the model. For open-hole model, zero effective stress on wellbore wall (since $\sigma_{rr}|_{r=R_w} = P_w$) is applied as a boundary load, while fixed boundary condition is applied on the wellbore wall ($u_r|_{r=R_w} = 0$). To simulate the effect of swelling strain, a thermal expansion domain is introduced in the solid mechanics module, where the reference temperature is defined as $\varepsilon^s_L b_L P_0/(1 + b_L P_0)$, representing the in situ conditions, and the temperature function

defined as $\varepsilon_{\mathrm{L}}^{\mathrm{s}} b_{\mathrm{L}} P/(1+b_{\mathrm{L}}P)$, representing the depleted reservoir conditions, with a coefficient of thermal expansion; that is $\overline{\varepsilon}_{\mathrm{v}}^{\mathrm{s}}/3$ as the thermal strain. With these conditions, we can replicate the exact same constraints as in the analytical solution. The model was discretised by the second order free triangular mesh. The model is a variation of the model used by Masoudian and Hashemi (2016) and Masoudian et al. (2018) (without the plasticity component).

Figs. 2 and 3 illustrate the cross-comparison of stress and displacement from the numerical and analytical solutions for the open-hole case, respectively. The radial profiles of stress and displacement were extracted at four different tangential coordinates ($\theta = 0°, 30°, 45°$ and $90°$, measured counter-clockwise from the positive x direction), all of which exhibit a good match. The same comparison is conducted for the lined-hole case as shown in Figs. 4 and 5, where a good match is also evident.

4.2. Results of the analysis for the illustrative example

Using the values in Table 1, the contours of stress and displacement were generated for a case where the reservoir fluid is

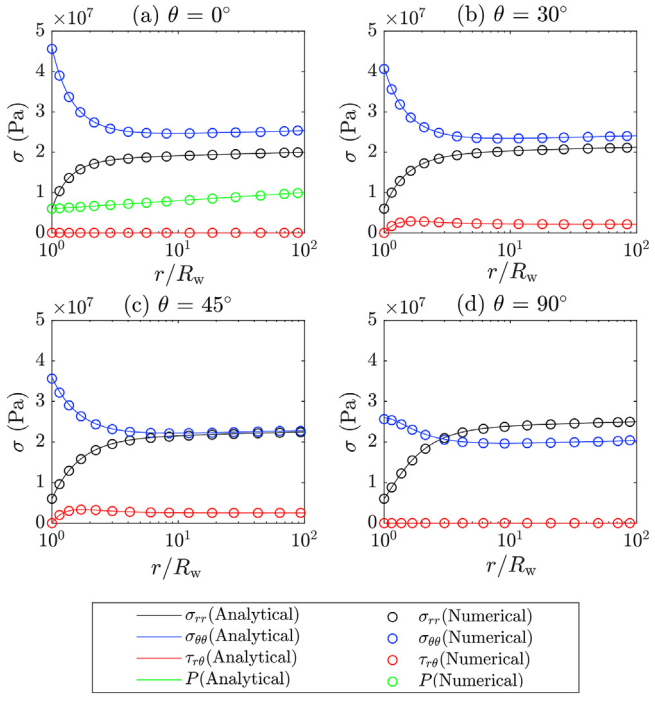

Fig. 2. Verification of the stress solutions for the open-hole case.

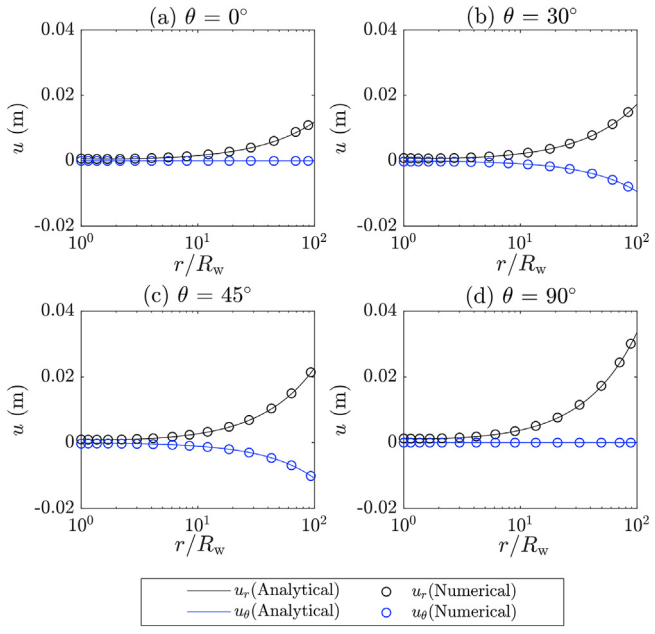

Fig. 3. Verification of the displacement solutions for the open-hole case.

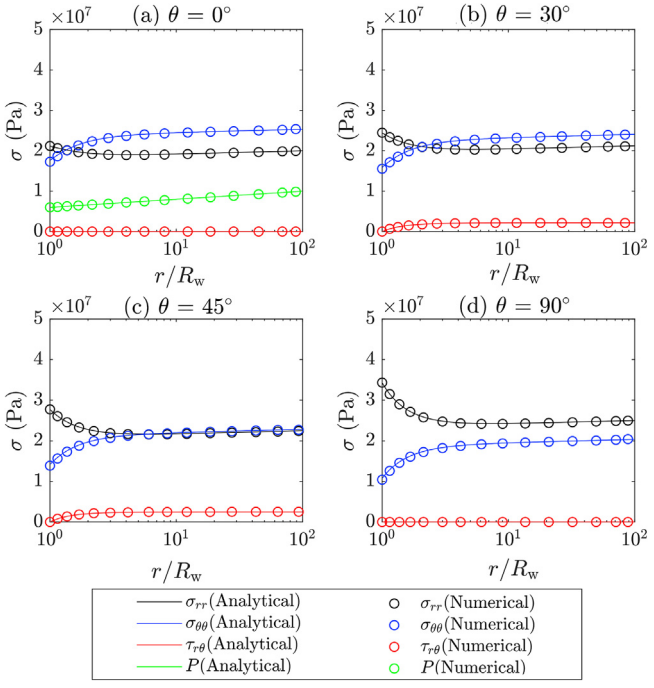

Fig. 4. Verification of the stress solutions for the lined-hole case.

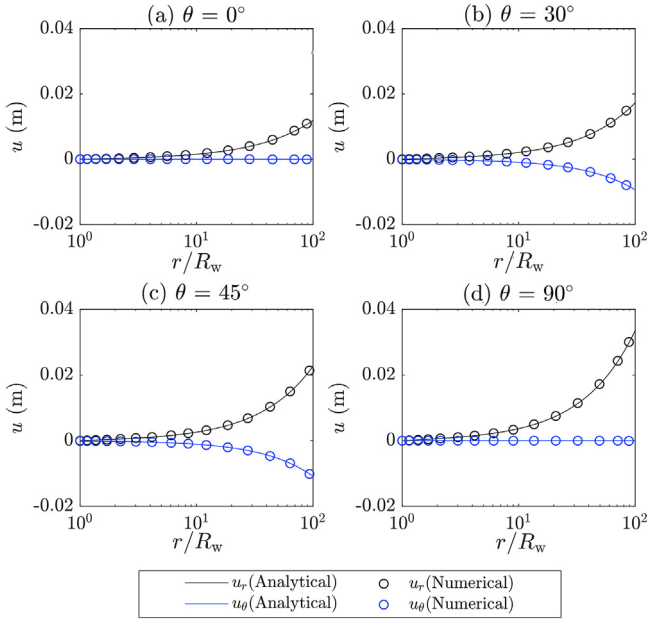

Fig. 5. Verification of the displacement solutions for the lined-hole case.

withdrawn from a reservoir through a wellbore. Figs. 6 and 7 plot the stress and displacement distributions for the open-hole case, respectively. As can be seen in Fig. 6, the radial stress is the minimum around the wellbore while the tangential stress is the maximum around the wellbore. On the wellbore wall, the maximum radial stress is found on the crown ($\theta = 90^\circ$) and invert ($\theta = 270^\circ$) of the wellbore, while the maximum tangential stress is found on the sides of the wellbore ($\theta = 0^\circ$ and 180°). Note that the maximum and minimum tangential stresses have the same magnitude but opposite signs, with the maximum occurring at $\theta = 45^\circ$ and 225°, and the minimum occurring at $\theta = 135^\circ$ and 315°. The shear stress is zero at 90° intervals (i.e. at $\theta = 0^\circ, 90^\circ, 180^\circ, 270^\circ$) where the transition between the positive and negative shear stress occurs. It can also be seen that both radial and tangential stress contours have both horizontal symmetry (y-axis is the line of symmetry) and vertical symmetry (x-axis is the line of symmetry), and the shear stress contours have two lines of symmetry at $\theta = 45^\circ$ and 135°. As evident from Fig. 7a and b, the tangential displacement is almost an order of magnitude smaller than its radial counterpart. It can also be seen that the displacement is larger in the y direction (Fig. 7c) corresponding to the larger in situ stress in the y direction, resulting in the convergence of the wellbore (Fig. 7d) into an elliptical shape.

The contours of stress and displacement for the lined-hole case are presented in Figs. 8 and 9, respectively. These figures are similar to those of the open-hole case with some general trends being identical (e.g. lines of symmetry), while there are some obvious differences discussed as follows. Similar to the open-hole case, the radial stress is the maximum at the crown and the invert, while the tangential stress is the maximum on the sides of the wellbore, but the magnitudes of stress are very different between the two cases. It should be noted, however, that in the lined-hole case, the major principal stress is the radial stress, while it is the tangential stress in open-hole case. The tangential stress distribution in lined-case hole is also very similar to that in open-hole case, but the magnitude of shear stress is slightly larger in the open-hole case. Fig. 9 also shows that, as imposed by the boundary condition, the wellbore wall shows no radial displacement, but the general displacement of the

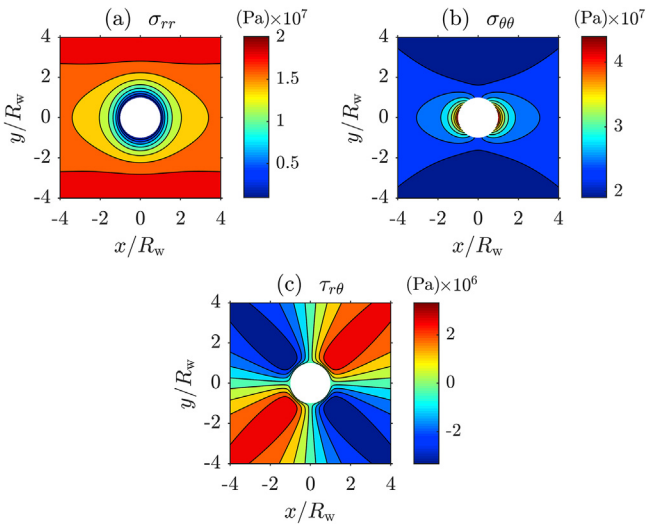

Fig. 6. Contours of stress in the open-hole case: (a) Radial stress, (b) Tangential stress, and (c) Shear stress.

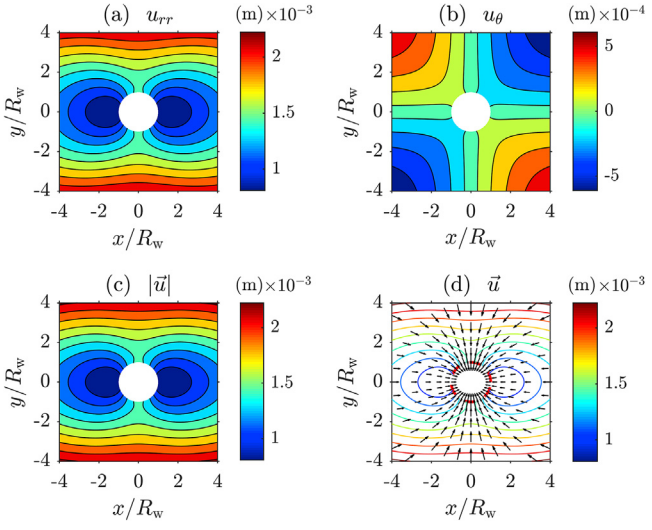

Fig. 7. Contours of displacement in the open-hole case: (a) Radial displacement, (b) Tangential displacement, (c) Magnitude of displacement vector field, and (d) Direction of the displacement vector field.

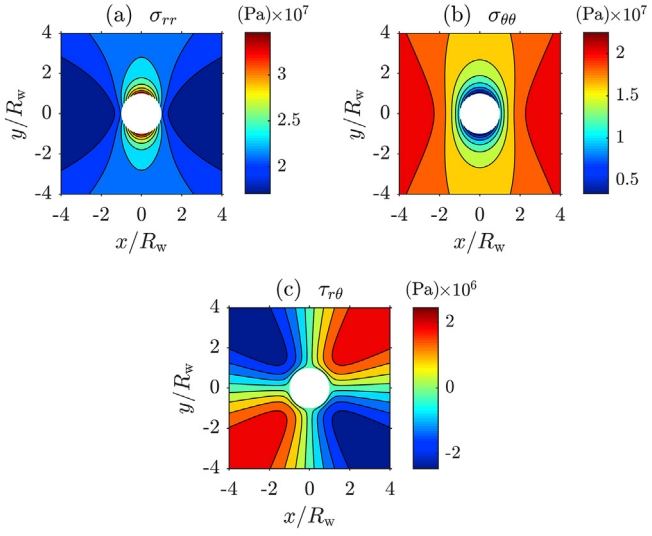

Fig. 8. Contours of stress in the lined-hole case: (a) Radial stress, (b) Tangential stress, and (c) Shear stress.

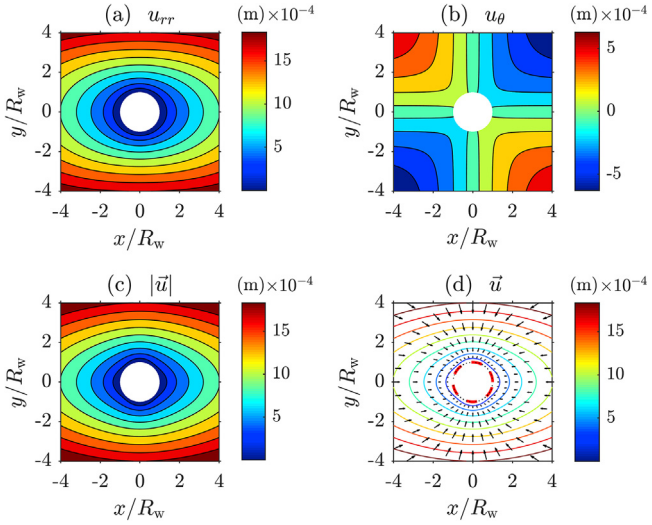

Fig. 9. Contours of displacement in the lined-hole case: (a) Radial displacement, (b) Tangential displacement, (c) Magnitude of displacement vector field, and (d) Direction of the displacement vector field.

rock is towards the wellbore, which is the result of smaller pore pressure (greater effective stress) near the wellbore.

The results presented in Figs. 6–9 are caused by the interaction of three different mechanisms, i.e. the effects of wellbore, fluid drainage, and desorption-induced shrinkage. Excavating or drilling a wellbore removes the support of effective in situ stress that formerly existed and tends to cause a displacement towards the centre of the wellbore. This also leads to changes in the stress concentration around the wellbore. This effect corresponds to Kirsch's problem of a hole in an infinite plate. Then, if the fluid is withdrawn through the wellbore, the non-uniform (radial) decrease of pore pressure causes an increase in the level of effective stress within the rock. If the pore pressure reduction is associated with swelling/shrinkage (sorption-induced in this study), the effective stress distribution can further change. In order to better understand these mechanisms and the role they play in the stress distribution around the wellbore, the example (both open-hole and lined-hole cases) was further investigated. First, the wellbore pressure was taken equal to the initial pore pressure ($P_w = P_0$) and the swelling factor was taken as zero ($\varepsilon_L^s = 0$), so that the illustrative example only represents the effect of wellbore. Then, by changing the value of P_w to that given in Table 1 and keeping $\varepsilon_L^s = 0$, the results include the effect of non-uniform pore pressure distribution. The original results, with the values of P_w and ε_L^s equal to those given in Table 1, represent the original example that includes all three effects. Using this approach, the role of these three effects in the distribution of stress concentration is analysed as illustrated in Fig. 10 for the open-hole case and in Fig. 11 for the lined-hole case. To simplify the comparison process, dimensionless isotropic (mean) effective and deviatoric stress components ($\tilde{p}'$ and $\tilde{q}$, respectively) are defined as

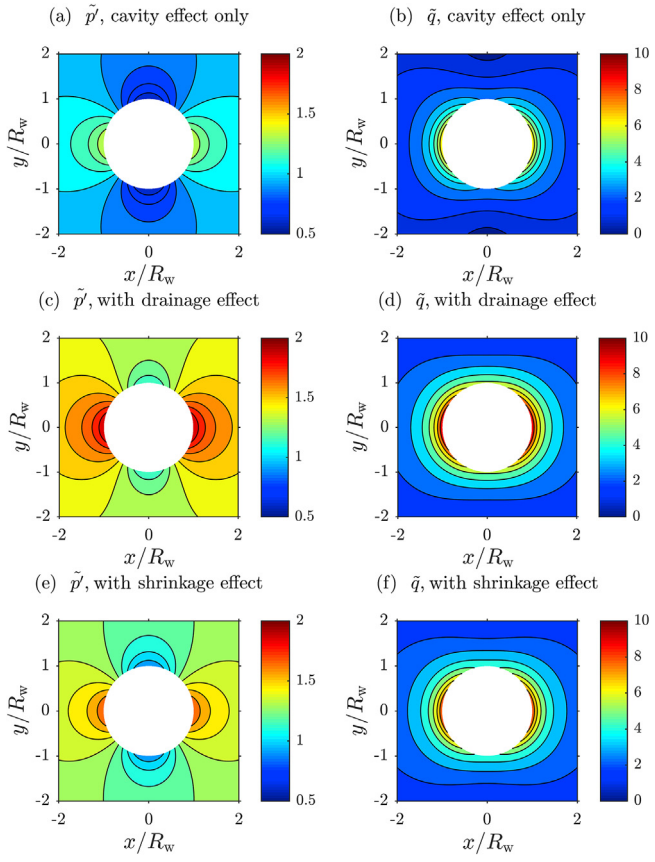

Fig. 10. The role of three different effects in stress concentration in the open-hole case: (a) Mean effective stress with wellbore effect only, (b) Deviatoric stress with wellbore effect only, (c) Mean effective stress with the drainage effect, (d) Deviatoric stress with drainage effect, (e) Mean effective stress with shrinkage effect, and (f) Deviatoric stress with shrinkage effect.

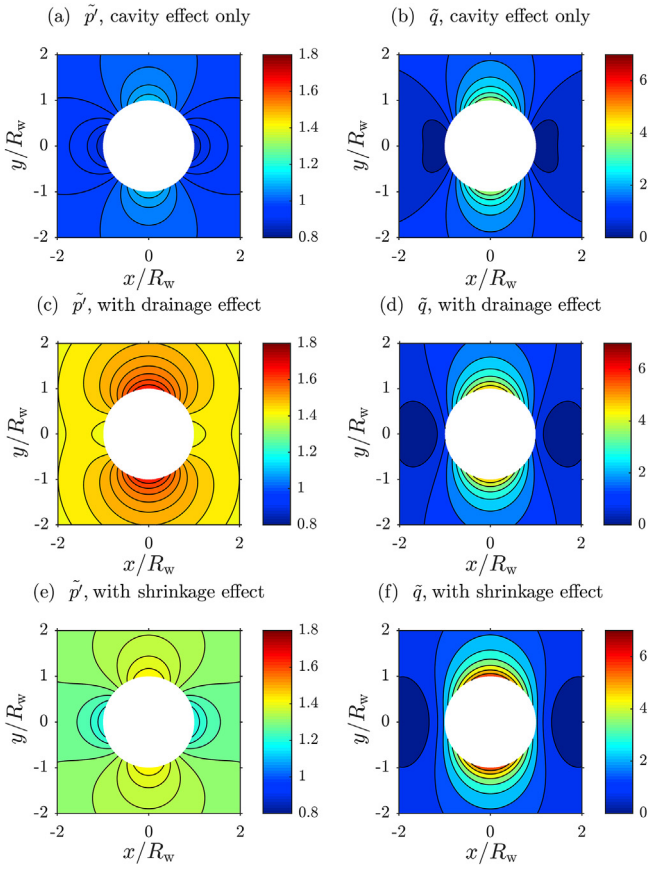

Fig. 11. The role of three different effects in stress concentration in the lined-hole case: (a) Mean effective stress with wellbore effect only, (b) Deviatoric stress with wellbore effect only, (c) Mean effective stress with drainage effect, (d) Deviatoric stress with drainage effect, (e) Mean effective stress with shrinkage effect, and (f) Deviatoric stress with shrinkage effect.

$$\tilde{p}' = \frac{\sigma'_1 + \sigma'_2}{\sigma'^0_1 + \sigma'^0_2} = \frac{\sigma'_{xx} + \sigma'_{yy}}{\sigma'^0_{xx} + \sigma'^0_{yy}} \tag{30a}$$

$$\tilde{q} = \frac{\sigma'_1 - \sigma'_2}{\sigma'^0_1 - \sigma'^0_2} = \frac{\sqrt{\left(\sigma'_{xx} - \sigma'_{yy}\right)^2 / 4 + \tau_{xy}^2}}{\left(\sigma'^0_{xx} - \sigma'^0_{yy}\right)/2} \tag{30b}$$

Note that the stress tensor conversion from polar coordinates to Cartesian coordinates, and vice versa, is given as (Bower, 2009):

$$\begin{bmatrix} \sigma_{xx} & \tau_{xy} \\ \tau_{xy} & \sigma_{yy} \end{bmatrix} = \begin{bmatrix} \cos\theta & -\sin\theta \\ \sin\theta & \cos\theta \end{bmatrix} \times \begin{bmatrix} \sigma_{rr} & \tau_{r\theta} \\ \tau_{r\theta} & \sigma_{\theta\theta} \end{bmatrix} \times \begin{bmatrix} \cos\theta & \sin\theta \\ -\sin\theta & \cos\theta \end{bmatrix} \tag{31a}$$

$$\begin{bmatrix} \sigma_{rr} & \tau_{r\theta} \\ \tau_{r\theta} & \sigma_{\theta\theta} \end{bmatrix} = \begin{bmatrix} \cos\theta & \sin\theta \\ -\sin\theta & \cos\theta \end{bmatrix} \times \begin{bmatrix} \sigma_{xx} & \tau_{xy} \\ \tau_{xy} & \sigma_{yy} \end{bmatrix} \times \begin{bmatrix} \cos\theta & -\sin\theta \\ \sin\theta & \cos\theta \end{bmatrix} \tag{31b}$$

For the open-hole case, Fig. 10a and b shows that, compared to the in situ stress state, the mean effective stress around the

wellbore increases on the sides of the wellbore ($\tilde{p}' > 1$), while it decreases around the top and the bottom of the wellbore ($\tilde{p}' < 1$). The deviatoric stress, however, increases significantly compared to the in situ condition. Comparing Fig. 10c and d with Fig. 10a and b shows an obvious increase in both mean effective stress and deviatoric stress when the effect of fluid drainage is considered. This is because the drainage of fluid, and consequently pore pressure reduction, lead to an increase in the level of effective stress within the continuum. Fig. 10e and f depicts the results, including the sorption-induced swelling, which show a reduction in the level of stresses. This is because the reduction of pore pressure leads to a negative swelling strain (shrinkage) in accordance with Langmuir's curve, which results in a lower stress concentration around the wellbore. Therefore, it is important to note that the pore pressure and swelling/shrinkage effects are acting in opposite directions and therefore compete with each other in the development of stress concentration around the wellbore. It should also be noted that a small volumetric shrinkage factor (1%) used in this example resulted in noticeable change in stresses, which underlines the significance of sorption-induced swelling/shrinkage in the mechanical response of the rock. Analysing Fig. 11 shows that the conclusions drawn for the open-hole case are still valid for the lined-hole case and the main difference is the relatively lower stress levels in the lined-hole case.

4.3. Parametric study: open-hole case

In order to better understand the effect of individual parameter on the results, a parametric study is conducted for the open-hole case using the developed analytical solution. The elastic modulus (E), sorption-induced swelling coefficient ($\varepsilon_{\mathrm{L}}^{\mathrm{s}}$), wellbore pressure ($P_{\mathrm{w}}$), and the minor initial principal stress (σ_{xx}^{0}) were chosen for this parametric study, where their values were changed one at a time and the remainder of the parameters remained constant. Fig. 12 depicts the sensitivity of the solution to the elastic modulus. It can be seen that larger elastic modulus results in lower stress levels, although this effect is more pronounced for the mean effective stress. A larger elastic modulus also leads to smaller displacement in both radial and tangential directions. This is because when analysing the stresses, the elastic modulus only impacts the swelling-related terms and a larger elastic modulus leads to a larger effect of shrinkage which, as discussed earlier, reduces the stress concentration. On the other hand, the smaller displacements with larger elastic modulus are consistent with classical elastic theory.

Fig. 13 shows the effect of Langmuir's swelling coefficient on the stress levels and displacements. The role of swelling/shrinkage and its impact on stress were discussed when describing the results in Fig. 10 and the same effect is observed here, i.e. reducing the stress level near the wellbore when increasing the swelling coefficient (Fig. 13a and b). However, further from the wellbore, this effect is somewhat diminished, and at some radial distance, this effect is slightly reversed. In order to explain this behaviour, it should be noted that the radial stress decreases throughout the whole reservoir domain with increasing swelling coefficient but this decrease becomes less noticeable at the far field. The tangential stress decreases with larger swelling coefficient near the wellbore, where the effects of wellbore and pore pressure change are more pronounced, but it starts to increase at some radial distance in response to larger radial compression of the reservoir. Thus, in the far field, the larger swelling coefficient leads to higher level of mean effective stress but this behaviour occurs at a much shorter distance for the deviatoric component of stress. It can also be seen that the radial displacement increases with larger swelling coefficient, while the tangential displacement remains unchanged. This is because the sorption-induced strain is considered to be isotropic,

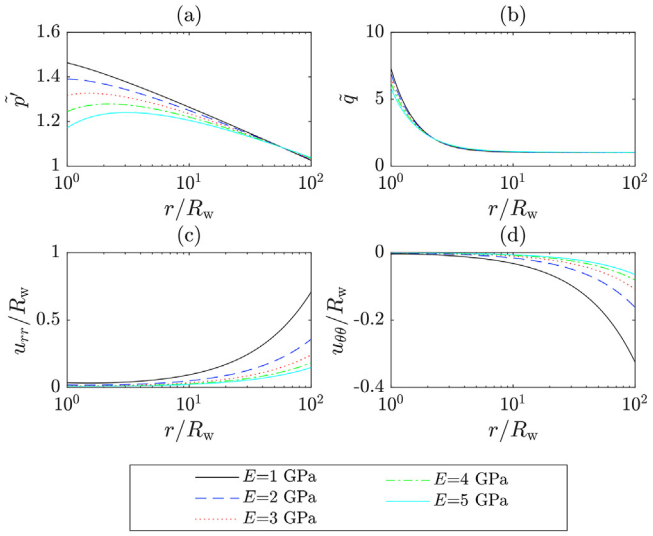

Fig. 12. Sensitivity of the open-hole solution to elastic modulus at $\theta = 45°$: (a) Mean effective stress, (b) Deviatoric stress, (c) Radial displacement, and (d) Tangential displacement.

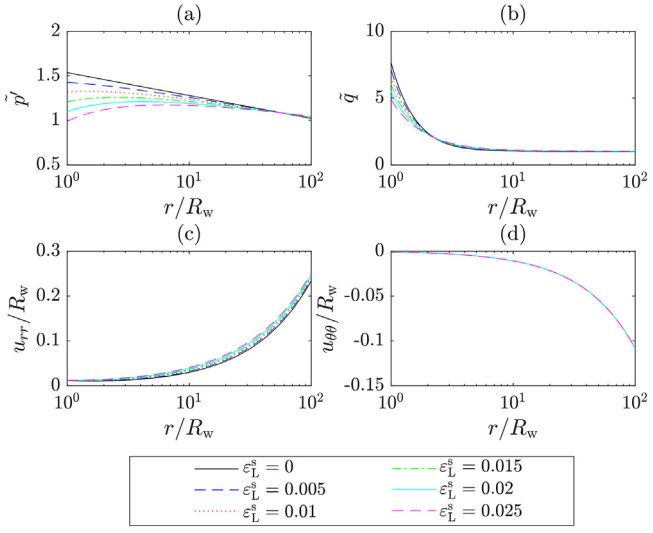

Fig. 13. Sensitivity of the open-hole solution to swelling coefficient at $\theta = 45°$: (a) Mean effective stress, (b) Deviatoric stress, (c) Radial displacement, and (d) Tangential displacement.

and therefore, it affects both the radial and the tangential components of the strain in the same way, and as such the tangential displacement remains constant with changing swelling coefficient.

The effect of wellbore pressure on the stress and displacement solutions is depicted in Fig. 14, and understanding its effect is somewhat simple. Lower well pressure leads to larger change in the pore pressure within the reservoir and hence higher effective stress levels (for both mean and deviatoric components). This leads to a slight increase of the radial displacement, but the tangential displacement remains unchanged as the gradient of pore pressure acts similar to a body load. Since flow is only radial, the tangential component of this body load is zero, and hence the tangential displacement is not affected by varying wellbore pressure.

The effect of the initial stress field on the solution is illustrated in Fig. 15. Note that in producing this figure, only σ_{xx}^{0} was changed while σ_{yy}^{0} remained constant to study the effect of the ratio of initial principal stresses. While it is obvious that increasing σ_{xx}^{0} leads to

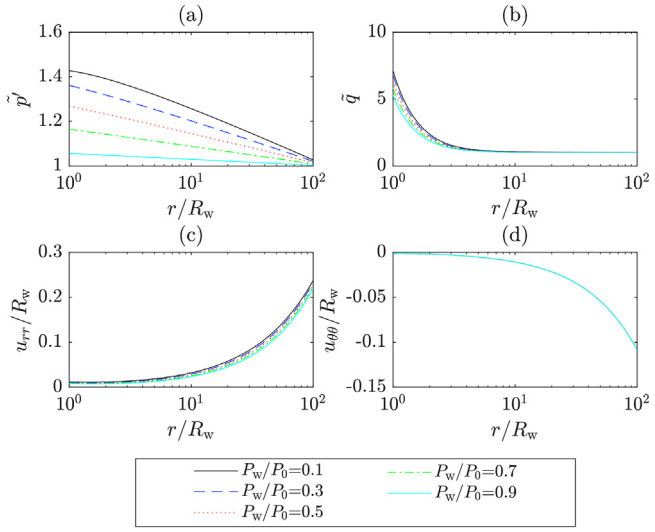

Fig. 14. Sensitivity of the open-hole solution to wellbore pressure at $\theta = 45°$: (a) Mean effective stress, (b) Deviatoric stress, (c) Radial displacement, and (d) Tangential displacement.

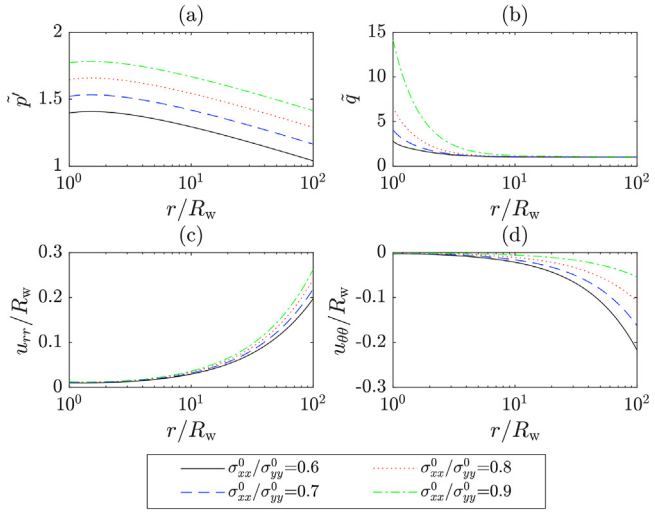

Fig. 15. Sensitivity of the open-hole solution to minor initial principal stress at $\theta = 45°$: (a) Mean effective stress, (b) Deviatoric stress, (c) Radial displacement, and (d) Tangential displacement.

larger mean stress level, the ratio of newly distributed stress to the larger initial mean stress reduces as seen in Fig. 15a. The larger σ^0_{xx} also lowers the deviatoric stress level, but this reduction is less than the reduction in the initial deviatoric stress level, resulting in larger deviatoric stress with larger σ^0_{xx} (Fig. 15b). In other words, when the initial stress field is more uniform, the deviation of the redistributed stress field compared to the initial stress field is comparatively larger (i.e. larger ratio of redistributed stress to initial stresses).

5. Conclusions

This paper presents the development of a poroelastic solution for a circular wellbore in a swelling rock under non-hydrostatic initial stress field. This analytical solution is relatively straightforward, compared to existing solutions in the literature, while considering the effect of sorption-induced swelling/shrinkage in the elastic constitutive equations. The analytical solution can be employed in a range of engineering applications, including unconventional gas reservoirs, which was used as an illustrative example. The solution was verified against a numerical model and the results were analysed for an example in which a gas producing wellbore was considered in a coalbed methane reservoir. Different physical phenomena contributing to redistribution of stress are identified and their individual significance is analysed. The results showed that a sorption-induced swelling coefficient as little as 1% can significantly influence the distribution of stresses within the reservoir and more importantly near the wellbore, which can have significant implications for the wellbore stability problem. While a steady-state solution for fluid flow has been used in this paper, the developed solution can be used with transient flow models by slight adjustment for incremental analysis. Poroelastoplastic formulations have recently been developed (Fokker et al., 2020), and thus this will be considered in future works along with shrinkage and swelling processes. This recommendation is very important for short-term analysis of wellbore where the drainage zone (R_0) changes with time or long-term analysis in infinite reservoirs. It is also suggested that the stress field in an unconventional reservoir can also play an important role in changing the permeability of these reservoir and the solution can also be used for such purpose.

Declaration of competing interest

The authors declare that they have no known competing financial interests or personal relationships that could have appeared to influence the work reported in this paper.

Acknowledgments

This work has been supported by the Advance Queensland Industry Research Fellowship (mid-career) scheme, the University of Queensland (UQ), and the proponents of the UQ Centre for Natural Gas (Australia Pacific LNG, Santos, and Arrow Energy).

List of symbols

Applied mechanics

$\sigma_{rr}, \sigma_{\theta\theta}, \sigma_{zz}, \tau_{r\theta}$	Stress components in cylindrical coordinates
σ_1, σ_2	Major and minor principal stresses in two dimensions
σ^0_{xx}	In situ stress in x direction under initial reservoir conditions
σ^0_{yy}	In situ stress in y direction under initial reservoir conditions
σ'	Effective stress
$\varepsilon_{rr}, \varepsilon_{\theta\theta}, \varepsilon_{r\theta}$	Strain components in polar coordinates
$\bar{\varepsilon}^s_v$	The sorption-induced volumetric strain
α	Biot's coefficient
Φ	Airey's stress function
ν	Poisson's ratio
$\bar{\nu}$	Plane-strain Poisson's ratio
E	Elastic modulus
$\bar{E}$	Plane-strain elastic modulus
G	Shear modulus
$\tilde{p}'$	Normalised mean effective stress
$\tilde{q}$	Normalised deviatoric stress
u_r, u_θ	Radial displacement in radial and tangential directions

Geometry

r, θ, z	Directions in cylindrical coordinates (the origin at the centre of the hole)
R_0	Half-length of the model
R_w	Radius of the wellbore

Flow and sorption parameters

P	Pore pressure (fracture porosity)
P_0	Uniform pore pressure in the reservoir under initial condition
P_w	Wellbore pressure (constant during gas production)
b_L	Reciprocal of Langmuir pressure
ε_L^s	Maximum sorption-induced volumetric swelling strain

Other definitions

∇^2	Laplacian operator
$\nabla^2\nabla^2 = \nabla^4$	Biharmonic operator
A, B, C, D	Constant coefficients. Subscripts p and s indicate terms related to pore pressure and swelling effects, respectively. Subscripts 1 and 2 indicate the terms related to the first and second invariants
S_1	A constant equivalent of the in situ effective mean stress
S_2	A constant equivalent to half of the in situ deviatoric stress
$f_1(r), f_2(r), f_p(r), f_s(r)$	Functions describing the effect of the first stress invariant, the second stress invariant, pore pressure and swelling, respectively
$F_p(r)$	A special integral function for pore pressure
$F_\varepsilon(r)$	A special integral function for sorption-induced strain

Appendices A, B, C. Supplementary data

Supplementary data to this article can be found online at https://doi.org/10.1016/j.jrmge.2021.05.003.

References

Abousleiman, Y., Nguyen, V., 2005. Poromechanics response of inclined wellbore geometry in fractured porous media. J. Eng. Mech. 131, 1170–1183.

Agheshlui, H., Sedaghat, M.H., Matthai, S., 2018. Stress influence on fracture aperture and permeability of fragmented rocks. J. Geophys. Res.: Solid Earth 123, 3578–3592.

Atefi-Monfared, K., Rybicki, J., 2018. Production versus injection induced poroelasticity surrounding wells. J. Petrol. Sci. Eng. 162, 102–113.

Bai, B., Li, T., 2009. Solutions for cylindrical cavity in saturated thermoporoelastic medium. Acta Mech. Solida Sin. 22, 85–94.

Bobet, A., 2001. Analytical solutions for shallow tunnels in saturated ground. J. Eng. Mech. 127, 1258–1266.

Bower, A.F., 2009. Applied Mechanics of Solids. CRC press.

Chen, G., Yu, L., 2015. Consolidation around a tunnel in a general poroelastic medium under anisotropic initial stress conditions. Comput. Geotech. 66, 39–52.

Connell, L.D., 2009. Coupled flow and geomechanical processes during gas production from coal seams. Int. J. Coal Geol. 79, 18–28.

Connell, L.D., Detournay, C., 2009. Coupled flow and geomechanical processes during enhanced coal seam methane recovery through CO2 sequestration. Int. J. Coal Geol. 77, 222–233.

Cui, X., Bustin, R.M., Chikatamarla, L., 2007. Adsorption-induced coal swelling and stress: implications for methane production and acid gas sequestration into coal seams. J. Geophys. Res.: Solid 112.

Day, S., Fry, R., Sakurovs, R., 2008. Swelling of Australian coals in supercritical CO_2. Int. J. Coal Geol. 74, 41–52.

Detournay, E., Cheng, A.H.D., 1988. Poroelastic response of a borehole in a non-hydrostatic stress field. Int. J. Rock Mech. Min. Sci. Geomech. Abstr. 25, 171–182.

Fahimifar, A., Tehrani, F.M., Hedayat, A., Vakilzadeh, A., 2010. Analytical solution for the excavation of circular tunnels in a visco-elastic Burger's material under hydrostatic stress field. Tunn. Undergr. Space Technol. 25, 297–304.

Fokker, P.A., Singh, A., Wassing, B.B.T., 2020. A semianalytic time-resolved poro-elasto-plastic model for wellbore stability and stimulation. Int. J. Numer. Anal. Methods GeoMech. 44, 1032–1052.

Ghassemi, A., Tao, Q., Diek, A., 2009. Influence of coupled chemo-poro-thermoelastic processes on pore pressure and stress distributions around a wellbore in swelling shale. J. Petrol. Sci. Eng. 67, 57–64.

Johansson, T.B., Patwardhan, A.P., Nakićenović, N., Gomez-Echeverri, L., 2012. Global Energy Assessment: toward a Sustainable Future. Cambridge University Press.

Jussila, P., 1997. Analytical solutions of the mechanical behaviour of rock with applications to a repository for spent nuclear fuel. Radiation and Nuclear Safety Authority. Finland, Helsinki.

Laubach, S.E., Marrett, R.A., Olson, J.E., Scott, A.R., 1998. Characteristics and origins of coal cleat: a review. Int. J. Coal Geol. 35, 175–207.

Liu, J., Chen, Z., Elsworth, D., Miao, X., Mao, X., 2010. Evaluation of stress-controlled coal swelling processes. Int. J. Coal Geol. 83, 446–455.

Liu, J., Chen, Z., Elsworth, D., Qu, H., Chen, D., 2011. Interactions of multiple processes during CBM extraction: a critical review. Int. J. Coal Geol. 87, 175–189.

Malvern, L.E., 1969. Introduction to the Mechanics of a Continuous Medium.

Masoudian, M.S., 2016. Multiphysics of carbon dioxide sequestration in coalbeds: a review with a focus on geomechanical characteristics of coal. J. Rock Mech. Geotech. 8, 93–112.

Masoudian, M.S., Airey, D.W., El-Zein, A., 2013a. Mechanical and flow behaviours and their interactions in coalbed geosequestration of CO2. Geomech Geoeng. Int. J. 8, 229–243.

Masoudian, M.S., Airey, D.W., El-Zein, A., 2013b. A chemo-poro-mechanical model for sequestration of carbon dioxide in coalbeds. Geotechnique 63, 235–243.

Masoudian, M.S., Airey, D.W., El-Zein, A., 2014. Experimental investigations on the effect of CO_2 on mechanics of coal. Int. J. Coal Geol. 128–129, 12–23.

Masoudian, M.S., El-Zein, A., Airey, D.W., 2016. Modelling stress and strain in coal seams during CO_2 injection incorporating the rock–fluid interactions. Comput. Geotech. 76, 51–60.

Masoudian, M.S., Hashemi, M.A., 2016. Analytical solution of a circular opening in an axisymmetric elastic-brittle-plastic swelling rock. J. Nat. Gas Sci. Eng. 35 (Part A), 483–496.

Masoudian, M.S., Hashemi, M.A., Tasalloti, A., Marshall, A.M., 2018. Elastic–brittle–plastic behaviour of shale reservoirs and its implications on fracture permeability variation: an analytical approach. Rock Mech. Rock Eng. 51, 1565–1582.

Masoudian, M.S., Leonardi, C., Chen, Z., Underschultz, J., 2019a. The Effect of Sorption-Induced Shrinkage on the Ground Surface Movement above Gas-Producing Coalbeds. In: Proceedings of the 53rd U.S. Rock Mechanics/Geomechanics Symposium.

Masoudian, M.S., Leonardi, C., Chen, Z., Underschultz, J., 2019b. Towards the development of a baseline for surface movement in the Surat Cumulative Management Area. The APPEA J 59, 95–114.

McGlade, C., Speirs, J., Sorrell, S., 2013. Unconventional gas – a review of regional and global resource estimates. Energy 55, 571–584.

Pan, Z., Connell, L.D., 2012. Modelling permeability for coal reservoirs: a review of analytical models and testing data. Int. J. Coal Geol. 92, 1–44.

Rawal, C., Ghassemi, A., 2014. A reactive thermo-poroelastic analysis of water injection into an enhanced geothermal reservoir. Geothermics 50, 10–23.

Sedaghat, M.H., Azizmohammadi, S., Matthäi, S.K., 2017. Numerical investigation of fracture-rock matrix ensemble saturation functions and their dependence on wettability. J. Petrol. Sci. Eng. 159, 869–888.

Shi, J.Q., Durucan, S., 2004. Drawdown induced changes in permeability of coalbeds: a new interpretation of the reservoir response to primary recovery. Transport Porous Media 56, 1–16.

Sulem, J., Panet, M., Guenot, A., 1987. An analytical solution for time-dependent displacements in a circular tunnel. Int. J. Rock Mech. Min. Sci. Geomech. Abstr. 24, 155–164.

Timoshenko, S., Goodier, J., 1951. Theory of Elasticity. McGraw-Hill book Company.

White, C.M., Smith, D.H., Jones, K.L., Goodman, A.L., Jikich, S.A., LaCount, R.B., DuBose, S.B., Ozdemir, E., Morsi, B.I., Schroeder, K.T., 2005. Sequestration of carbon dioxide in coal with enhanced coalbed methane recovery: a review. Energy Fuel. 19, 659–724.

Wong, H., Morvan, M., Deleruyelle, F., Leo, C.J., 2008. Analytical study of mine closure behaviour in a poro-elastic medium. Comput. Geotech. 35, 645–654.

Zare Reisabadi, M., Haghighi, M., Salmachi, A., Sayyafzadeh, M., Khaksar, A., 2020. Analytical modelling of coal failure in coal seam gas reservoirs in different stress regimes. Int. J. Rock Mech. Min. Sci. 128, 104259.

Zareifard, M.R., Fahimifar, A., 2015. Elastic–brittle–plastic analysis of circular deep underwater cavities in a mohr-coulomb rock mass considering seepage forces. Int. J. GeoMech. 15, 04014077.

Zhang, J., Bai, M., Roegiers, J.C., 2003. Dual-porosity poroelastic analyses of wellbore stability. Int. J. Rock Mech. Min. Sci. 40, 473–483.

Zhang, R., Winterfeld, P.H., Yin, X., Xiong, Y., Wu, Y.-S., 2015. Sequentially coupled THMC model for CO_2 geological sequestration into a 2D heterogeneous saline aquifer. J. Nat. Gas Sci. Eng. 27, 579–615.

Mohsen S. Masoudian holds a PhD in Geomechanics from the University of Sydney (Australia), a Master of Petroleum Engineering from Curtin University (Australia), and a Bachelor of Mining Engineering and Rock Mechanics from Shahid Bahonar University of Kerman (Iran). Mohsen is currently a Senior Rock Mechanics Engineer at Beck Engineering, where he uses his expertise to help design, optimise, and maintain some of the world's largest mining and energy projects. Prior to his current industrial role, Mohsen spent several years in academic environment, working as a Research Fellow at the University of Queensland (Australia) and as a Postdoctoral Research Associate at the University of Nottingham (United Kingdom). Having worked on a wide range of experimental, theoretical and field studies concerned with geomechanical aspects associated with extractive industries, he has acquired significant expertise in coupled processes in geomechanics.